Wave, current and bottom topographical interactions in the coastal ocean bottom boundary layer

Aditya R.Nayak[1], Cheng Li[1], Bobak Kiani[1] and Joseph Katz[1]

[1] Department of Mechanical Engineering, Johns Hopkins University, Baltimore, USA
anayak2@jhu.edu

ABSTRACT

A submersible PIV system has been deployed to characterize mean flow and turbulence in the inner part of the coastal ocean bottom boundary layer (BBL), and their interaction with the bottom roughness. Five large datasets, each consisting of ~20,000 velocity distributions, are chosen for analysis to represent flow conditions spanning a range of relative wave-current magnitudes, and ripple height and orientations. In each case, vertical distributions of mean velocity, Reynolds stresses, production and dissipation rates and spatial energy spectra have been determined. In cases where the amplitude of wave induced motions are similar or greater in magnitude to the mean current, there is an inflection point in the mean velocity profile, presumably at the interface of the thin wave boundary layer (WBL) and the much wider mean current boundary layer. Furthermore, the so-called "hydrodynamic roughness" felt by the current boundary layer, as determined from the mean profiles, is substantially larger than that determined from the measured roughness characteristics. When the current is more than 70% larger than the wave amplitude, the inflection disappears, and the hydrodynamic roughness falls below the measured values. As expected, velocity profiles vary from point to point within one roughness height away from the bottom, but collapse at higher elevations. The Reynolds shear stress profiles peak at the lower portion of the log layer, and decrease with increasing elevation further above. The Reynolds stress profiles do not collapse when scaled using either the wall unit or the roughness height as length scales. The shear production rate profiles appear to form three distinct groups based on relative wave-current magnitude and roughness orientation with the mean flow, peaking either at the top of the roughness elements or just above the inflection point. In most cases, production and dissipation converge within the log layer, but trends differ below it. Spatial energy spectra exhibit bumps at wavenumbers corresponding to 1-3 roughness heights, which are indicative of excess small scale energy produced by interaction of large scale turbulence with the roughness. With decreasing elevations, spectra become increasingly anisotropic, and an inertial range develops only at low wavenumbers at high elevations.

1. INTRODUCTION

A vertical section of the water column in the coastal ocean is composed of three distinct regions– a surface mixed layer, a bottom boundary layer (BBL) and a central stratified region which separates the two. The coastal ocean BBL constitutes a relatively small portion of the water column. However, being a zone of increased mass and momentum transfer, it plays an important role in ocean dynamics, influencing various processes such as sediment transport, shelf circulation, tidal energy balances, and nutrient mixing [1]. Hence, a thorough understanding of the mechanisms that drive the BBL as well as small scale processes that occur within, is essential.

The current BBL is tidally driven, with the vertical scale of the order of a few meters. In addition to the current, surface waves can influence flow all the way to the seabed in water depths up to roughly half their wavelength [2]. In the coastal ocean, this condition is readily satisfied. Thus, the flow develops under the combined influence of waves and current, with a thin oscillatory boundary layer forming just above the seabed. The short time scales of the waves limit this wave boundary layer (WBL) to a few cm thick, highly sheared region. Typically, under mild to moderate wave conditions, the WBL height is expected to range from 1-5 cm, although it can grow thicker than 10 cm in wave dominated flows [1]. Within this embedded region, the turbulence statistics are expected to be associated with both the current and waves, whereas outside, shear associated with the current predominantly generates the turbulence.

Laboratory studies over both smooth and rough walls, in purely oscillatory and combined wave-current flows, have been carried out to simulate the BBL dynamics [3-6]. Some interesting observations include the enhancement of the roughness in the presence of waves [4], and the deviation of the mean velocity profiles in combined flows from that expected by a linear superposition of waves and current [5]. Field data is essential for complementing these studies in order to account for non-collinear waves and current, inhomogeneous bottom ripples, and the large differences in length scales between oceanic current and wave boundary layers, which are impossible to reproduce in the laboratory. However, obtaining reliable field data on the flow structure and turbulence in the inner part of the often misaligned combined wave-current bottom boundary layer over a rippled bottom is a challenging task. Hence, there have only been a handful of measurements resolving the flow and turbulence within the BBL [7-13] leading to a paucity of data to draw meaningful conclusions from. Typically used oceanographic instruments to quantify turbulence are ADVs, ADCPs, and pulse coherent Doppler profilers, which are either point sensors, or provide 1D distribution, with the resolution of the most advanced instruments ranging from 1-10 cm. Consequently, our group has been involved in applications of PIV to resolve the flow in the inner part of the BBL, achieving sub cm resolution over a sample area of 30x30 cm^2 that extend from the bottom [13-17]. Other recent oceanic applications of PIV include systems mounted on a profiling platform [18], on tripods [19], and small-scale portable devices [20]. This paper describes the results of recent measurements in which a massive PIV database enables us to obtain detailed statistics of the flow and turbulence combined with local characterization of the bottom roughness.

2 FIELD MEASUREMENTS

2.1 Submersible PIV system

A schematic of the submersible 2D PIV system is shown in Figure 1. The system has been modified several times over the last 15 years, since it was first deployed by our group [13-17], and apart from the PIV units, hosts an array of ancillary instruments, as described below. In its present form, it consists of two separate PIV units, which can be aligned independent of each other. The light source is a ship-board flashlamp pumped dye laser operating at a wavelength of 595 nm. For each unit, the light is transmitted to the submerged platform through a 400 µm optical fiber connected to a submerged probe containing the requisite optics to generate a 4-5 mm thick light sheet. Images are recorded at 12 frames/s by Imperx© 2048 x 2048 pixels^2 interline transfer CCD cameras, which are enclosed in underwater housings. Naturally present particles (e.g., phytoplankton) are used as flow tracers, and they are typically abundant enough to obtain 5-10 particle pairs per interrogation window [14]. The typical particle size is smaller than 50 µm. Larger particles, which might be associated with e.g. swimming zooplankton, are typically removed from the images before the data are analyzed. The PIV images obtained are converted to an optical signal and transferred to a RAID hard drive array located on board the research vessel. The platform also contains an acoustic doppler velocimeter (ADV), located upstream of the PIV planes, whose sampling volume is 2.6 cm^3. A short burst of data from this sensor is used to determine the mean flow and dominant wave direction, and align the PIV sample areas accordingly, typically aligning one sheet with the mean current, and the other with waves if they are inclined. The ADV data also facilitates removal of the wave induced motion from the velocity, which is essential for Reynolds shear stress calculations, as elucidated in §3.2. A high resolution (2 mm) pencil beam sonar equipped with an azimuth drive is used to obtain 2D cross sectional profiles of the bottom topographical structure at different angles, hence providing information about the height and alignment of the bottom ripples to the flow. Other instruments include a high precision pressure sensor, a biaxial inclinometer, two video cameras, and a digital compass. The entire package is mounted on a turntable which allows the system to be oriented remotely to minimize flow misalignment. Once the required orientation is achieved, magnets clamp the system in place and eliminate any potential disturbances to it during data acquisition.

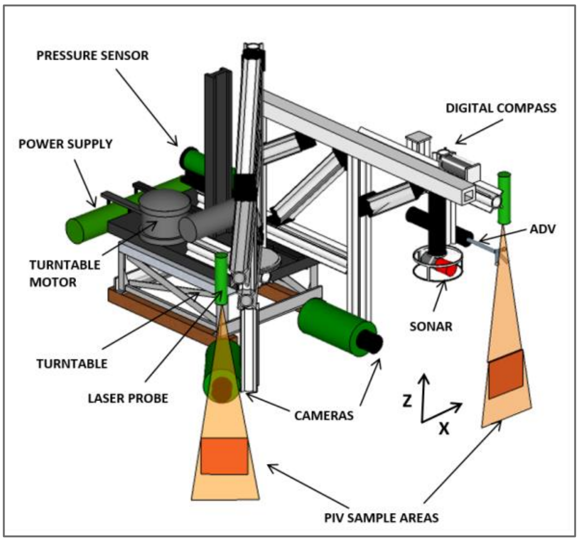

Figure 1 Schematic of the submersible PIV system

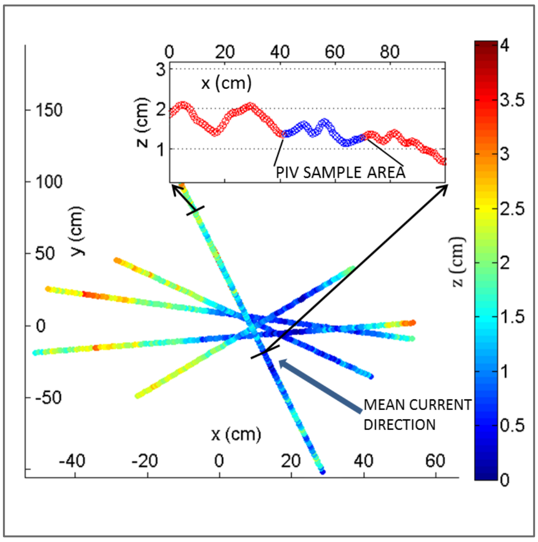

Figure 2 Sample sonar transects of bottom topography for run 1. The location of the PIV field of view is indicated.

The submersible system was deployed over two consecutive summers in 2011 and 2012, off the Atlantic coast near LEO-15, a coastal ocean observatory maintained by Rutgers University, at depths varying from 19 to 21 m. Statistics of the wave-induced motions obtained from the ADV data indicated that the rms value of wave orbital velocities (u^w_{rms}) ranged from 6-11 cm s^{-1}, their periods fell in the 7.5-13 s range, corresponding to wavelengths of 80-170 m. The significant wave heights varied from 40-56 cm, and are calculated as $H_{sig} = 4\sigma_\eta$, where σ_η is the standard deviation of the sea surface displacement [21]. For the sets used in this paper, the mean current varied from 5 to 22 cm/s. We recorded several datasets spanning different portions of the tidal cycle, under varying relative wave-current-bottom topographical orientations. The PIV & ADV data were sampled at 6 and 16 Hz respectively. During each PIV run, at least 5 sonar bottom transects at different orientations were carried out to map the bottom topography. Each dataset spanned 30-60 minutes, corresponding to 11800 - 21600 2D instantaneous velocity distributions for each sample area. The PIV field of view (FOV) was 28.8x28.8 cm^2 and 29.4x29.4 cm^2 during the two deployments respectively, with the seabed being visible in the images in the majority of the datasets obtained. The acquired images were initially enhanced using a modified histogram equalization algorithm [22], and objects larger than 16 pixels were removed. The cross-correlations to generate the velocity vector maps were carried out using an in-house developed code [22]. A multi-pass procedure was used with a final correlation window size of 64 x 64 pixels^2 and 50% overlap between adjacent windows. This process yielded 2D velocity fields containing typically 62 x 62 vectors with vector spacing of 4.5 mm, and with the bottom-most vector located ~5 mm off the seabed.

Results obtained from 5 datasets are discussed in this paper. Three of these runs are from the most recent field experiments described above. However runs 4 and 5 are from a prior deployment in the same site, which has been discussed in detail by Hackett et al [13]. Some of those findings are presented here to compare them with the other runs and facilitate discussion on the effect of different wave-current-ripple conditions on the mean flow and turbulence statistics. Table 1 provides a brief summary of the flow conditions, scaling and turbulence parameters involved.

Run	$\bar{u}$ (cm/s)	u^w_{rms} (cm/s)	$\bar{u}/u^w_{rms}$	u^*_{fit} (cm/s)	$z^* = \upsilon/u^*_{fit}$ (mm)	$\sqrt{-u'w'_m}$ (cm/s)	z_{0fit} (cm)	z_{0meas} (cm)	$\frac{z_{0fit}}{z_{0meas}}$	Alignment to ripples
1	15.2	8.9	1.71	0.75	0.15	0.75	0.21	0.42	0.50	Normal
2	14.6	8.4	1.74	0.64	0.17	0.62	0.19	0.42	0.45	Normal
3	22.6	11	2.05	1.21	0.09	1.17	0.94	2.92	0.32	Parallel
4	5.0	8.0	0.60	0.34	0.32	0.31	1.09	0.28	3.89	Unknown
5	5.9	7.7	0.77	0.44	0.25	0.34	1.01	0.28	3.61	Unknown

Table 1 Mean flow and turbulence parameters during presented runs.

3 RESULTS

3.1 Bottom topography

For runs 1-3, obtained during the most current deployments, the bottom topography is mapped using a pencil beam sonar. The sonar provides bottom transects at different planes perpendicular to the seafloor. At each plane, the sonar sweeps the same transect at least 30 times to reduce the uncertainty in measurement to within 2 mm. The number of sweeps at each transect is based on laboratory calibrations over a sand bed. The same procedure is repeated to obtain at least 5 different transects of lengths varying from 0.8 -1.6 m, the longest of which coincides with the PIV measurement plane. The data from the runs over a few successive hours is then concatenated to generate a distribution of the seafloor roughness. Sample sonar data for run 1 is presented in figure 2. In runs 1 & 2, acquired during 2011, the ripple height (α), measured crest to trough is 2 ± 0.5 cm, its wavelength Λ is 90 cm, and the mean current direction is perpendicular to the ripples. For the 2012 tests, for which run 3 is a sample, α=5 ± 1.2 cm, Λ=80 cm and the mean current is parallel to the ripple crest (not shown). Run 3 represents this case. We do not have sonar data available for the earlier runs (4 and 5). Visual observations based on the intersection of the light sheet with the bottom in the PIV images [13] indicate that the ripple dimensions are α ~1 cm and Λ ~ 33 cm.

3.2 Mean velocity profiles

Non-dimensionalized mean velocity profiles are presented in Figure 3. In all cases, a clear log layer is evident. The familiar log law is given by

$$\frac{\bar{u}(z)}{u^*_{fit}} = \frac{1}{\kappa} \ln \frac{(z - z_{ref})}{z_{0fit}} \quad (1)$$

where $\overline{u}(z)$ is the ensemble averaged velocity, u^*_{fit} is the friction velocity, z_{ref} is the reference height, z_{0fit} is the hydrodynamic roughness, and κ is the von Karman constant and is taken to be 0.41. In our results, z=0 corresponds to the ripple crest, and z_{ref} is chosen to obtain a clearly defined log region, which represents a co-ordinate shift to a point located a few mm below the ripple crest. The values of u^*_{fit} and z_{0fit} are obtained by a least squares fit to the data points in the log region. The normalized elevation is $z^+ = \frac{(z-z_{ref})u^*_{fit}}{\nu}$, where ν is the kinematic viscosity and all the profiles are collapsed by shifting them by $\frac{1}{\kappa} ln z^+_{0fit}$. Below the log layer, the profiles diverge and trends vary with $\overline{u}/u^w_{rms}$, roughness height and orientation, as well as location of measurement point relative to the roughness.

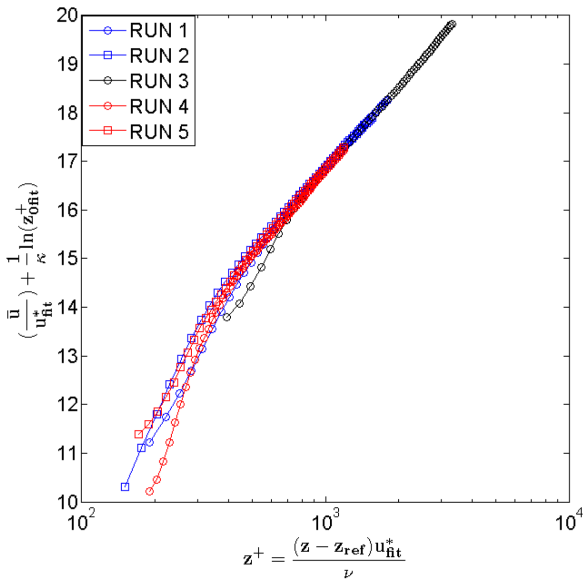

Figure 3 Normalized mean velocity profiles, all runs.

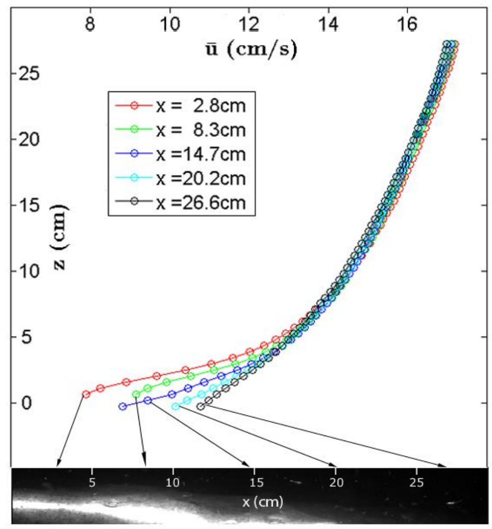

Figure 4 Mean velocity profiles for run 3, different streamwise locations.

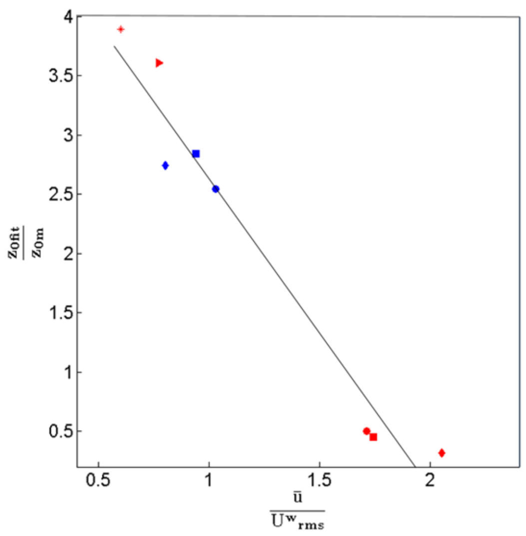

Figure 5 Variation of z_{0f}/z_{0m} with $\overline{u}/u^w_{rms}$. Results for runs 1-5 (Table 1) are indicated by red points, while blue symbols indicate data from additional runs.

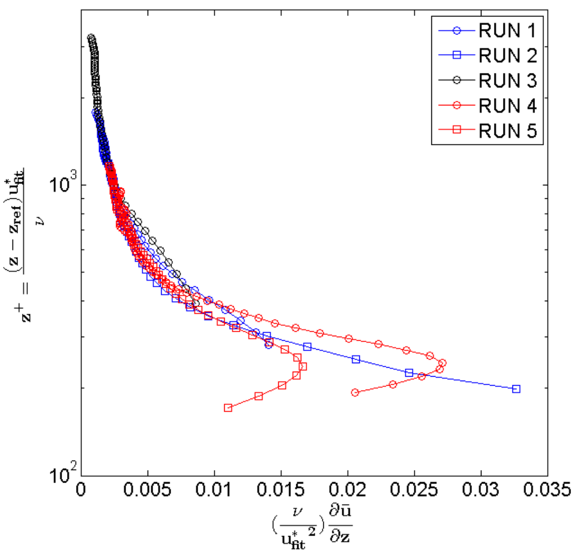

Figure 6 Normalized vertical shear profiles, all runs.

To demonstrate the effect of roughness on the mean flow, profiles at different stream-wise locations in the same PIV measurement plane (run 3) are illustrated in Figure 4, with a sample image of the seabed superimposed. No significant variations in profiles occur within the log layer. However, within 6 cm off the seabed, i.e., ~1.2α, they vary substantially, being lowest above the ripple crests and higher in other locations at the same elevation, consistent with rough wall laboratory measurements [23].

The hydrodynamic roughness can be estimated in two ways: The first method, as described above, involves finding the intercept to the least square fit to the log region of the velocity profile, and is referred to here as z_{0fit} . The second method entails using the actual bottom ripple characteristics measured using the sonar. Here, we use the semi-empirical relationship proposed by Grant and Madsen [24] to obtain the ripple roughness k_b as a function of the ripple height and wavelength

$$k_b = 28\frac{\alpha^2}{\Lambda} \tag{2}$$

Following Jimenez [25], the hydrodynamic roughness z_{0m}, can be estimated from

$$z_{0meas} = \frac{k_b}{30} \tag{3}$$

Figure 5 compares the trends of z_{0fit}/z_{0meas} with variations in relative wave-current magnitude, i.e., $\bar{u}/u^w_{rms}$, including three additional runs, which are not discussed further here. A clear pattern emerges: when the amplitudes of wave induced motion are of similar or higher magnitude than the currents, ($\bar{u}/u^w_{rms} \leq 1$), z_{0fit}/z_{0m} ~2.5-3.9, implying that the waves seem to play a role in enhancing the roughness felt by the flow in the current boundary layer. These observations agree with prior wave-current interaction studies in tidally driven BBL flows [12]. Conversely, under dominant current conditions ($\bar{u}/u^w_{rms}$ >1.7, runs 1-3), z_{0fit}/z_{0meas} varies from 0.3-0.5. A least squares fit to the data points (R^2 =0.95) suggests a linear trend.

To further elucidate the effects of $\bar{u}/u^w_{rms}$ on the mean current, Figure 6 shows the profiles of mean streamwise velocity gradients ($\partial\bar{u}/\partial z$), with the non-dimensionalized elevation plotted on a log scale to highlight the near wall behavior. For $\bar{u}/u^w_{rms}$ >1.7, $\partial\bar{u}/\partial z$ monotonically increases with decreasing elevation, peaking at the top of the ripples, as expected. Conversely, for $\bar{u}/u^w_{rms}$ < 1, an inflection point is evident at z^+ = 235-245. Inflection points are typically seen to occur in regions of flow instabilities, e.g., at the top of the canopy in atmospheric boundary layer flows over vegetation [26], in rough wall boundary layers at peak of roughness elements [27-28], and in mixing layers [29].These inflection points are characterized by increased turbulence levels, and indeed, in all the above examples [26-29], the Reynolds shear stresses, production and dissipation peak there. The corresponding turbulence statistics in our observations, and their trends in the region of the inflection (when present) are detailed in the subsequent sub-sections.

3.3 Reynolds stress profiles and scaling issues

The Reynolds shear stress calculations for coastal ocean data are difficult due to the inherent complications in separating unsteady motions induced by the presence of surface waves from the turbulence [1, 30-31]. The wave induced motion should not generate Reynolds stresses, but a slight misalignment between the PIV coordinate system and the wave propagation direction leaves a large signature in the correlation among the horizontal and vertical velocity components. Consequently, the wave-induced motion should be filtered out from the time-resolved data before calculating the Reynolds shear stress. Several techniques have been utilized over the years to overcome this problem, [30-33].We use the linear adaptive filtering technique proposed by Shaw & Trowbridge [31] to address this issue. This method utilizes the velocity signal from two sensors, the PIV and the ADV data in our case, that are spatially separated by a distance much smaller than the wavelength of the wave, but larger than the integral turbulent length scale. As a result, the wave induced velocities should be coherent at the two locations, whereas the turbulence is not. This procedure implicitly assumes that the wave induced motion and turbulence are uncorrelated, a reasonable assumption outside of the wave boundary layer, but clearly incorrect near the seabed, where the waves interact with the roughness elements. By calculating the coherent part among the two sensors,$\tilde{u}$, we obtain an estimate for the wave velocity, which is then subtracted from the instantaneous velocity to obtain the turbulent fluctuations, and yield the Reynolds shear stress,

$$\overline{u'w'(z)} = \overline{[u(z,t) - \tilde{u}(z,t) - \bar{u}(z)][w(z,t) - \bar{w}(z)]} \tag{4}$$

Vertical profiles of Reynolds shear stress normalized by their respective maximum values, are presented in figure 6. To non-dimensionalize the vertical scales, one could use several relevant length scales, e.g., z_{0fit}, z_{0meas} or z^* (Table 1). When the elevation is scaled with z_{0meas}, the profiles do not collapse (Figure 7a), and though the trends are reversed, no collapse occurs when z^* is used as the scaling parameter instead (Figure 7b). Results do not collapse when z_{0fit} is used as well (not shown). The profiles appear to be separated into three distinct groups, the first with $\bar{u}/u^w_{rms}$ >1.7 and ripples oriented perpendicular to the mean current (runs 1 and 2), the second with $\bar{u}/u^w_{rms}$ > 1.7 (run 3) and ripples oriented parallel to the mean current, and the last group with $\bar{u}/u^w_{rms}$ < 1 (runs 4 and 5). For run 3, where the profile deviates the most from others, the ripple height is substantial (~ 5 cm). It is worth noting that we do not have any means of quantifying the boundary layer thickness δ, from our measurements, and consequently, could not use it as a length scale. For flow conditions with large roughness heights (e.g., run 3), it is possible that the condition for a "well-characterized" boundary layer, i.e., $\delta \geq 50\alpha$ [25], might not be satisfied. However, the length scales of ripples seen in run 3 represent common coastal bottom topographical conditions. Given the conflicting trends, one could try a mixed scaling parameter, e.g., $z_{0meas}^{\beta}(\nu/u_{fit}^{*})^{1-\beta}$, where $0<\beta<1$. This approach combines the effect of roughness with the boundary layer inner variables. For $\beta = 0.3$, we obtain a reasonable collapse in the profiles for all the present runs (Figure 7c). This is a simplistic approach, and should be considered as work in progress which does not take into account effects such as mean flow and wave orientation with respect to the ripples, which most likely are important.

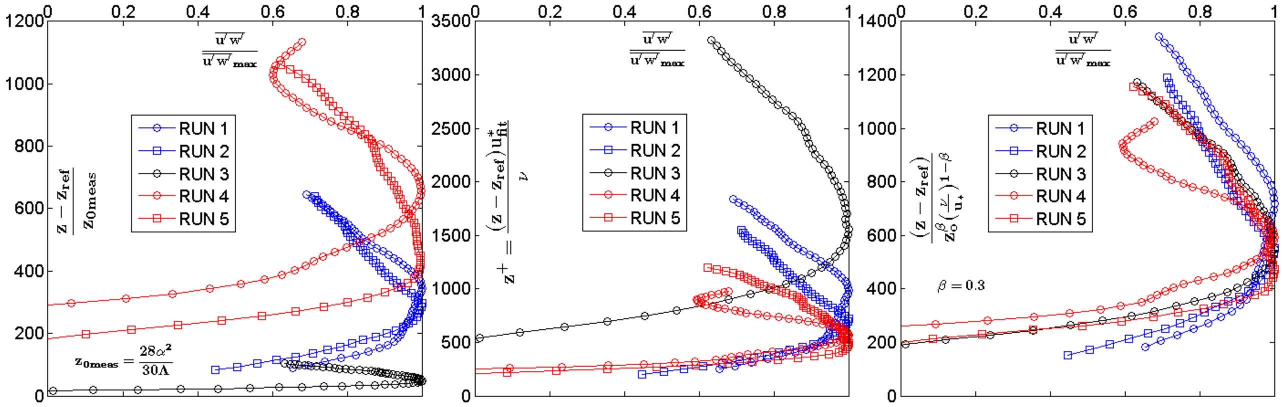

Figure 7 Vertical Reynolds shear stress profiles, with elevation normalized using (a) z_{0meas}, (b) υ/u_{fit}^{*} and (c) mixed scaling $z_{0meas}^{\beta}(\nu/u_{fit}^{*})^{1-\beta}$, with $\beta = 0.3$. In all cases, the horizontal axis is normalized by the individual peak stress values.

For all cases, the Reynolds shear stresses peak in the lower part of the log layer region. Above this peak, the stresses decrease with increasing elevation, and there is no evidence for a constant stress region commonly assumed in oceanic measurements. The ratio of peak shear stress to the friction velocity, $\frac{\sqrt{-\overline{u'w'}_m}}{u_{fit}^{*}} = 0.78 - 1.0$ for the different runs, consistent with laboratory and computational data for steady turbulent boundary layers [34]. The largest deviations of $\sqrt{-\overline{u'w'}_m}$ from u_{fit}^{*} occur when $\overline{u}/u_{rms}^{w}<1$ (Table 1). Below the maximum, the shear stresses decrease rapidly as the seafloor is approached. For runs 4 and 5 ($\overline{u}/u_{rms}^{w} < 1$), the Reynolds stress gradients peak near the inflection point, indicating that the maximum momentum depletion induced by the turbulence occurs here. For the other runs, $\partial(-\overline{u'w'})/\partial z$ peaks at the lowest point of measurement. Very near the seabed, the Shaw and Trowbridge method fails due to the fact that the waves interact with the bottom to generate turbulence, hence leading to a breakdown in the inherent assumption that turbulence and wave induced motions are uncorrelated.

3.4 *TKE shear production and dissipation estimates*

The spatial velocity gradients are used to estimate the dissipation rate, ε. Since only the in-plane gradients are available from the PIV data, we compute $\partial v/\partial y = -(\partial u/\partial x + \partial v/\partial z)$ using the continuity equation. The statistics of the other unmeasured terms are assumed to be equal to averages of the measured ones [17]. These assumptions lead to the following expression for the dissipation rate.

$$\varepsilon(x,z) \cong 4\upsilon\left[\overline{\left(\frac{\partial u}{\partial x}\right)^2 + \left(\frac{\partial w}{\partial z}\right)^2 + \frac{3}{4}\left(\frac{\partial u}{\partial z}\right)^2 + \frac{3}{4}\left(\frac{\partial w}{\partial x}\right)^2 + \left(\frac{\partial u}{\partial x}\right)\left(\frac{\partial w}{\partial z}\right) + \frac{3}{2}\left(\frac{\partial u}{\partial z}\right)\left(\frac{\partial w}{\partial x}\right)}\right] \quad (5)$$

The accuracy of the dissipation estimates depends on whether the PIV resolution is sufficient to resolve the turbulence completely [35-36]. For the data presented here, depending on the mean flow speed and elevation, the Kolmogorov scale $\eta = (\nu/\varepsilon)^{1/4}$ ranges from 0.5 to 1.4 mm. In other words, the PIV resolution varies between 2.5 – 8.5η. Lavoie et al [35] summarize the effect of PIV resolution on dissipation estimates for isotropic turbulence, and provide information that we could use to quantify the effect of resolution on dissipation estimates, at least for isotropic turbulence. Following this procedure, for our resolution range, attenuation varies from 25-65% for η = 1.4 to 0.5 mm respectively, and we use these factors to correct the estimates of dissipation rate. The TKE shear production rate is calculated using

$$P = -\overline{u'w'}\frac{\partial \bar{u}}{\partial z} \tag{6}$$

Dissipation and shear production rate profiles normalized by u_{fit}^{*3}/z_{0meas}, are plotted in Figure 8. We normalize the depth using the mixed scaling discussed above. The profiles do not collapse, irrespective of the scaling parameter used. Within the log layer, dissipation rate profiles seem to converge (Figure 8a). Below the log layer, the dissipation increases rapidly with decreasing elevation, peaking at the lowest measurement point. The production rate profiles (Figure 8b) differ significantly in both magnitude and trends, and as in the case of the shear stress profiles, could be divided into three distinct groups. For runs 1 and 2, i.e. when the mean flow is dominant, the production peak is located at the top of the roughness elements, consistent with laboratory rough wall measurements [23] and DNS results [27]. Conversely, for run 3, the peak is located higher up, at the bottom of the log layer, while for runs 4-5 ($\bar{u}/u_{rms}^{w} < 1$), it is located just above the inflection point, where the flow is expected to be unstable [26-29]. Sample production and dissipation profiles from each of the three groups are reproduced and compared in Figure 8c. For runs 1 and 2, P > ε near the bottom, in agreement with rough wall laboratory and DNS data [23, 27]. For runs 4-5 ($\bar{u}/u_{rms}^{w} < 1$), P and ε show opposite trends, with the former decreasing below the inflection point, and the latter increasing. In all cases, but run 3, P and ε converge in the log layer. In run 3, however, P is greater than ε throughout the log layer portion located within our range of measurements. This discrepancy might likely be associated with the large roughness elements for run 3, for which, the highest point of measurement is only five roughness heights.

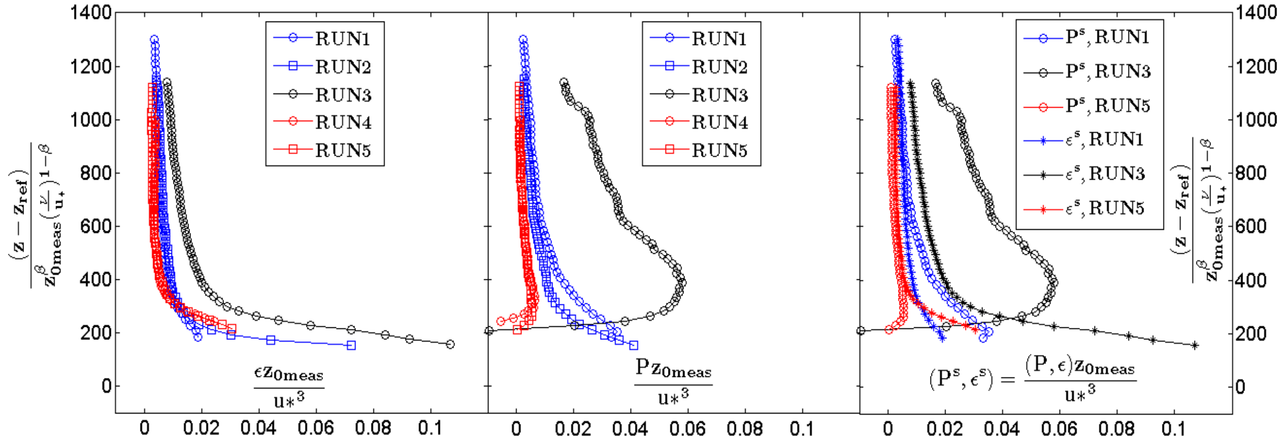

Figure 8 Vertical TKE shear production and dissipation profiles with elevation normalized using mixed scaling $z_{0meas}^{\beta}(\nu/u_{fit}^{*})^{1-\beta}$, and horizontal axis scaled with u_{fit}^{*} and z_{0meas}.(a) Scaled dissipation (b) Scaled production and (c) Sample scaled production and dissipation rate profiles to represent the three distinct groups that are observed.

3.5 Spatial energy spectra

This section examines trends of spatial energy spectra with elevation and roughness scales. The spectra are calculated along streamwise lines of instantaneous PIV data. The data are detrended before applying a fast Fourier transform, without any additional windowing function. The output is then ensemble averaged to obtain $E_{11}(k_1, z)$ and $E_{33}(k_1, z)$ for the streamwise and bed normal velocity components, respectively. Sample plots for two runs that represent different roughness conditions are presented in Figure 9. The spectra are scaled using $\upsilon^{5/4}\varepsilon(z)^{1/4}$at the corresponding elevation, and the wavenumber is non-dimensionalized using the elevation dependent Kolmogorov scale. For run 5, within the log region, the scaled spectra collapse, as seen in Figure 9a. A -5/3 slope is apparent, and $E_{11}(k_1)$ ~ (3/4) $E_{33}(k_1)$, which suggest the presence of an inertial range ($E_{33}(k_1)$ for run 5 is shown in Figure 10). The inclined dashed lines in the figure correspond to length scales of 1α and 3α, and they are sloped due to variations in η(z). A distinct spectral bump appears in $E_{11}(k_1)$ in the $2\pi/3\alpha < k_1\eta < 2\pi/\alpha$ range, i.e., at wavenumbers corresponding to 1-3 roughness heights. These bumps indicate excess small-scale energy, beyond the level resulting from energy cascading in isotropic turbulence. These bumps have been observed during our earlier deployments [16-17], but their origin has been an unexplained issue. However, recent laboratory rough wall spectra exhibit similar bumps at similar wavenumbers, which originate from the roughness [23]. These eddies are generated as large scale turbulence interacts with the roughness, and consequently, bypasses the cascading process. Similar phenomena have been reported for canopy turbulence [26]. These eddies are then entrained by outer layer vortical structures, and transported rapidly away from the wall. Thus, the concentration of roughness scale eddies in the outer region exceeds the number usually produced locally by the cascading process, hence giving rise to the spectral bumps. Below 7.5 cm away from the wall the spectra exhibit increasing anisotropy, and accordingly, the contribution of small scale turbulence, especially in the 1-3α range increases, as expected. In the laboratory, the roughness scale eddies fall in the dissipation range of the turbulent spectrum (α/η ~ 15-22) thus enhancing the dissipation rate over a broad area. For run 5, α/η ~ 9-17, i.e., the eddies also fall in the dissipation range, and most likely enhance the dissipation in the outer layer. For run 3 (Figure 9b), with larger roughness height, the spectra at the lowest elevations (z<5 cm, i.e., z<α) display a distinct bump at a wavenumber corresponding to α. However, the bump vanishes at higher elevations, where the turbulence becomes isotropic rapidly. In this case, α = 70-125η, i.e., the roughness scale eddies fall well outside the dissipation range, and they break down presumably by the energy cascading process. These sample trends suggest that the "longevity" (distinct signature) of roughness scale eddies with increasing distance from the wall depends on whether they fall in the dissipation or inertial ranges.

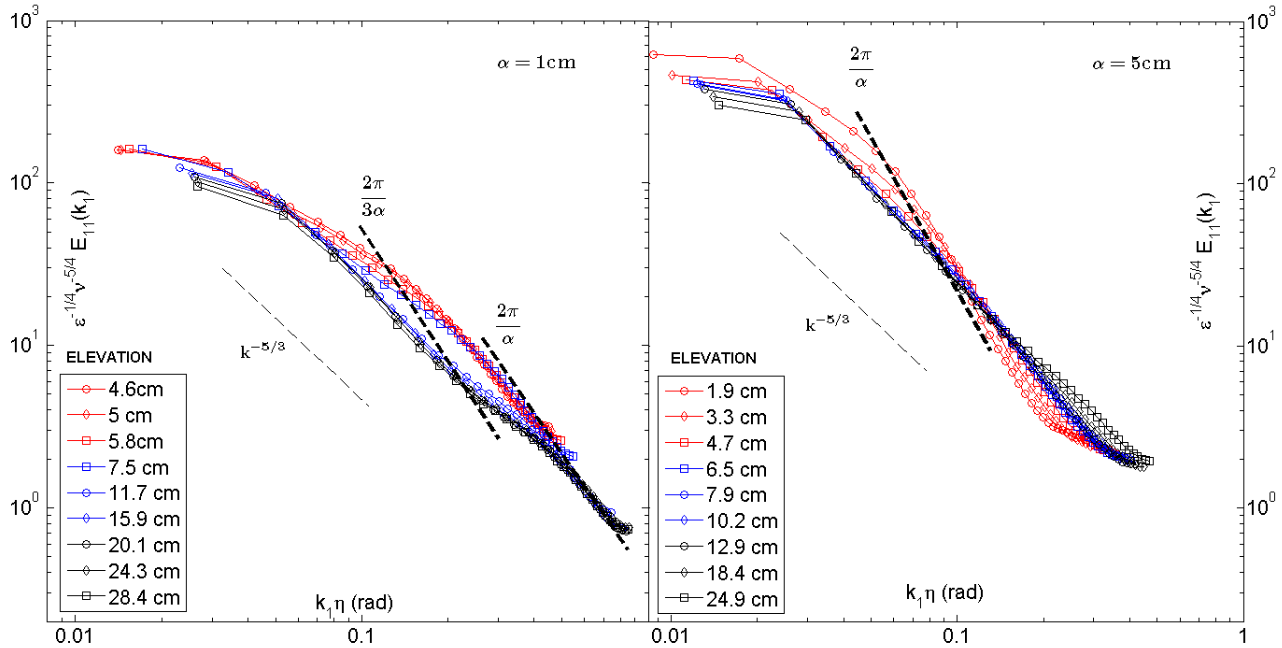

Figure 9 Ensemble averaged $E_{11}(k_1)$ spectra for (a) Run 5 and (b) Run 3. Spectra are normalized by the elevation dependent dissipation rate ε(z) and viscosity, while the wavenumbers are scaled with the elevation dependent Kolmogorov scale, η (z).

4. SUMMARY AND CONCLUSIONS

In this paper, we present results and discuss trends exhibited by five statistically converged PIV datasets obtained in the inner part of the coastal ocean BBL. These datasets span a range of flow conditions, with varying relative tidal current to wave induced velocity amplitude, bottom roughness, and ripple alignment with the flow. At upper elevations, the mean velocity profiles for all the runs indicate the presence of a log layer, where all the scaled profiles collapse. Near the wall, as expected, the profiles deviate. Wave-dominated cases ($\bar{u}/u^w_{rms} < 1$) are characterized by two distinct phenomena - an inflection point that appears below the log layer, and an increase in the apparent roughness felt by the overlying flow. In the current-dominated cases ($\bar{u}/u^w_{rms} > 1.7$), $\partial\bar{u}/\partial z$ monotonically increases with decreasing elevation with no inflection point.

Attempts to normalize the Reynolds stress, shear production and dissipation rates using relevant boundary layer and roughness length scales do not produce collapsed profiles. However, when scaled with z_{0meas} and u^*_{fit}, they appear to separate into three distinct groups, depending on relative wave-current magnitude, roughness height and/or flow alignment to the ripples. Since trends with z_{0meas} and u^*_{fit} are opposite, mixed scaling can be used for collapsing the data, but this conclusion is not sufficiently robust to generalize. All the Reynolds stress profiles peak at the bottom of the log region, steadily decreasing with increasing elevation above this maximum. The peak shear stress values, $\sqrt{-\overline{u'w'}_m}$ range from 0.78-1.0 u^*_{fit}, consistent with prior observations [34]. The minimum values of $\frac{\sqrt{-\overline{u'w'}_m}}{u^*_{fit}}$ are seen in cases where $\bar{u}/u^w_{rms} < 1$, and peaks of stress gradients coincide with the inflection point. In cases with $\bar{u}/u^w_{rms} > 1.7$ and with mean flow perpendicular to the ripples, production and dissipation rate trends are in agreement with those seen in rough wall laboratory and DNS data, i.e., they peak at the top of the roughness elements. On the other hand, when

$\bar{u}/u^w_{rms} < 1$, the production peaks occur at higher elevations, just above the inflection point. Thus, formation of an inflection, which according to Hackett et al [13] occurs at the interface between the wave and current boundary layers, impacts the production of turbulence and associated stresses. In all cases, but run 3, P/ε ~ 1 within the log region. In run 3, where $\bar{u}/u^w_{rms} > 1.7$, and the mean flow is parallel to the particularly large ripples, P peaks at the bottom of the log layer, and is greater than ε by at least a factor of two. This discrepancy is currently not fully understood, but might simply be a result of the PIV sample area extending only to 5α. Three dimensional (out of plane) interactions and contributions to production and dissipation rates might also be important.

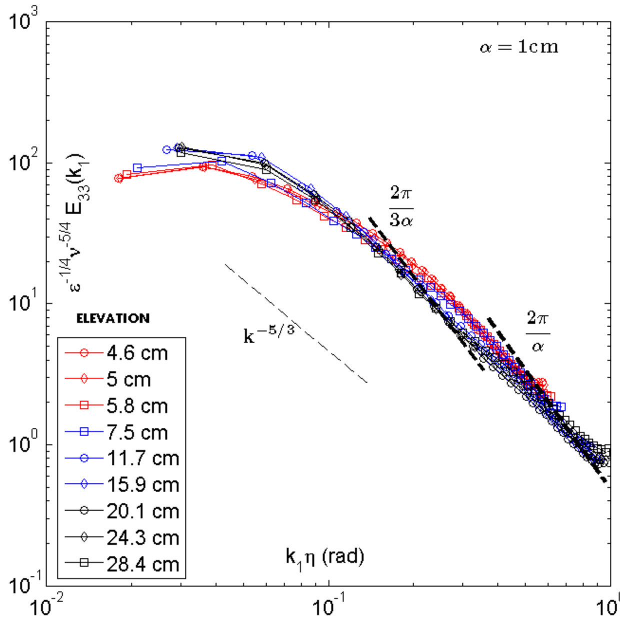

Figure 10 Ensemble averaged $E_{33}(k_1)$ spectra for Run 5. Spectra are normalized by the elevation dependent dissipation rate ε(z) and viscosity, while the wavenumbers are scaled with the elevation dependent Kolmogorov scale, η (z).

Spatial energy spectra within the log layer exhibit a wavenumber range with -5/3 slope and $E_{11}(k_1)$ ~ (3/4) $E_{33}(k_1)$, indicating an inertial range. When the roughness length scales fall within the dissipation range, distinct spectral bumps are observed at all elevations at wavenumbers corresponding to 1-3α, but their contribution increases with decreasing distance from the wall. Such bumps, also seen in recent laboratory rough wall studies, are the product of interaction of large scale turbulence with the ripples. When the roughness scales fall within the inertial range, the distinct roughness signature is limited to about one roughness height away from the wall.

Acknowledgements

This research is sponsored by National Science Foundation grant # OCE 1031040.The authors would like to thank Stephen King, Yury Ronzhes and the crew of the R/V Hugh R Sharp for their valuable assistance in testing and deploying the submersible system during the recent field trips.

REFERENCES

[1] Grant WD and Madsen OS "The continental shelf bottom boundary layer" Annual Review of Fluid Mechanics 18 (1986) pp.265-305

[2] Dean RG and Dalrymple RA "Water Wave Mechanics for Engineers and Scientists" World Scientific (1991)

[3] Sleath JFA "Turbulent oscillatory flow over rough beds" Journal of Fluid Mechanics 182 (1987) pp.369-409

[4] Fredsoe J, Andersen KH and Sumer BM "Wave plus current over a ripple-covered bed" Coastal Engineering 38 (1999) pp.177-221

[5] Kemp PH and Simons RR "The interaction between waves and a turbulent current: Waves propagating with the current" Journal of Fluid Mechanics 116 (1982) pp.227-250

[6] Kemp PH and Simons RR "The interaction of waves and a turbulent current: Waves propagating against the current" Journal of Fluid Mechanics 130 (1983) pp.73-89

[7] Caldwell DR and Chriss TM "The viscous sublayer at the seafloor" Science 205(4411) (1979) pp.1131-1132

[8] Conley DC and Inman DL "Field observations of the fluid-granular boundary layer under near-breaking waves" Journal of Geophysical Research 97 (1992) pp.9631-9643

[9] Trowbridge JH and Agrawal YC "Glimpses of a wave boundary layer" Journal of Geophysical Research 100 (1995) pp. 20,729-20,743

[10] Foster DL, Beach RA and Holman RA "Turbulence observations of the nearshore wave bottom boundary layer" Journal of Geophysical Research 11 (2006) C04011

[11] Zou Q, Bowen AJ and Hay A "Vertical distributions of wave shear stress in variable water depth: Theory and field observations" Journal of Geophysical Research 111 (2006) C09032

[12] Green MO, Rees JM, and Pearson ND "Evidence for the influence of wave-current interaction in a tidal boundary layer", Journal of Geophysical Research 95 (1990) pp. 9629-9644

[13] Hackett EE, Luznik L, Nayak AR, Katz J, and Osborn T " Field Measurements of turbulence at an unstable interface between current and wave boundary layers" Journal of Geophysical Research 116 (2011) C02022

[14] Bertuccioli L, Roth GI, Katz J and Osborn TR "A submersible particle image velocimetry system for turbulence measurements in the bottom boundary layer" Journal of Atmospheric and Oceanic Technology 16 (1999) pp.1635-1646.

[15] Smith WAMN, Atsavapranee NP, Katz J and Osborn TR "PIV measurements in the bottom boundary layer of the coastal ocean" Experiments in Fluids 33 (2002) pp.962-971

[16] Smith, WAMN, Katz J and Osborn TR "On the structure of turbulence in the bottom boundary layer of the coastal ocean" Journal of Physical Oceanography 35 (2005) pp.75-93

[17] Luznik L, Gurka R, Nimmo Smith WAM, Zhu W, Katz J and Osborn T "Distribution of energy spectra, Reynolds stresses, turbulence production and dissipation in a tidally driven bottom boundary layer." Journal of Physical Oceanography 37 (2006) pp.1527-1550

[18] Steinbuck JV, Roberts PLD, Troy CD, Horner-Devine AR, Simonet F, Uhlman AH, Jaffe JS, Monismith SG and Franks PJS "An autonomous open-ocean stereoscopic PIV profiler." Journal of Atmospheric and Oceanic Technology 27 (2010) pp.1360-1378

[19] Liao Q, Bootsma HA, Xiao J, Van Klump J, Hume A, Long MH and Berg P "Development of an in situ underwater particle image velocimetry (UWPIV) system" Limnology and Oceanography: Methods 7 (2009) pp.169-184

[20] Tritico HM, Cotel AJ and Clarke JN "Development, testing and demonstration of a portable submersible miniature particle imaging velocimetry device." Measurement Science and Technology 18 (2007) 2555-2562

[21] Holthuijsen LH "Waves in Oceanic and Coastal Waters" Cambridge University Press (2007)

[22] Roth GI and Katz J "Five techniques for increasing the speed and accuracy of PIV investigation" Measurement Science Technology 16 (2001) pp.1568-1579

[23] Hong J, Katz J and Schultz M "Near-wall turbulence statistics and flow structures over three-dimensional roughness in a turbulent channel flow" Journal of Fluid Mechanics 667 (2011) pp.1-37

[24] Grant WD, and Madsen OS "Movable bed roughness in unsteady oscillatory flow", Journal of Geophysical Research 87 (1982) pp.469–481

[25] Jimenez J "Turbulent flows over rough walls" Annual Review of Fluid Mechanics 36 (2004) pp.173-196

[26] Finnigan J "Turbulence in plant canopies" Annual Review of Fluid Mechanics 32 (2000) pp.519-571

[27] Ikeda T and Durbin PA "Direct simulations of a rough-wall channel flow" Journal of Fluid Mechanics 571 (2007) pp.235-263

[28] Raupach MR, Antonia AR and Rajagopalan S "Rough-wall turbulent boundary layers" Applied Mechanics Reviews 44 (1991) pp. 1-25

[29] Townsend AA "The Structure of Turbulent Shear Flow" Cambridge University Press (2010)

[30] Trowbridge JH "On a technique for measurement of turbulent shear stress in the presence of surface waves" Journal of Atmospheric and Oceanic Technology 15 (1998) pp.290-298

[31] Shaw WJ, and Trowbridge JH "The direct estimation of near bottom turbulent fluxes in the presence of energetic wave motions" Journal of Atmospheric and Oceanic Technology 18 (2001) pp.1540–1557

[32] Feddersen F and Williams III, AJ "Direct estimates of the Reynolds stress vertical structure in the nearshore" Journal of Atmospheric and Oceanic Technology 24 (2007) pp.102-116

[33] Bricker JD and Monismith SG "Spectral wave-turbulence decomposition" Journal of Atmospheric and Oceanic Technology 24 (2007) pp.1479-1487

[34] Pope SB "Turbulent Flows" Cambridge University Press (2000)

[35] Lavoie P, Avallone G, De Gregorio F, Romano GP and Antonia RA "Spatial resolution of PIV for the measurements of turbulence" Experiments in Fluids 43 (2007) pp.39-51

[36] Xu D and Chen J "Accurate estimate of turbulent dissipation rate using PIV data" Experimental Thermal and Fluid Science 44 (2013) pp.662-672